Colloids and Surfaces A: Physicochemical and Engineering Aspects 660 (2023) 130805

Contents lists available at ScienceDirect

Colloids and Surfaces A: Physicochemical and Engineering Aspects

journal homepage: www.elsevier.com/locate/colsurfa

Phosphate removal by $Ca(OH)_2$-treated natural minerals: Experimental and modeling studies

Dimitris Mitrogiannis [a], Maria Psychoyou [a], Ioannis Baziotis [a], Constantinos Mavrogonatos [b], Nikolaos Koukouzas [c], Ioannis Anastopoulos [d], Marios Fyrillas [e], Vassilis J. Inglezakis [f,*]

[a] Department of Natural Resources Management and Agricultural Engineering, Agricultural University of Athens, Iera Odos 75, 11855 Athens, Greece
[b] Faculty of Geology and Geoenvironment, National and Kapodistrian University of Athens, Panepistimiopolis, 15784 Athens, Greece
[c] Centre for Research and Technology Hellas (CERTH), Chemical Process and Energy Resources Institute (CPERI), 52 Egialias str., Maroussi, 15125 Athens, Greece
[d] Department of Agriculture, University of Ioannina, 47100 Kostakii Arta, Greece
[e] Frederick University, Department of Mechanical Engineering, 7 Y. Frederickou str., 1036 Nicosia, Cyprus
[f] Chemical & Process Engineering Department, University of Strathclyde, 16 Richmond St., Glasgow G1 1XQ, United Kingdom

HIGHLIGHTS

- Oversimplified diffusion-based models are widely used in batch adsorption studies.
- Phosphate adsorption kinetics on granular modified zeolite and bentonite was analysed.
- Emphasis was given on a slow approach to adsorption equilibrium lasting weeks.
- A non-dimensional two-phase homogeneous surface diffusion model (TP-HSDM) was applied.
- Internal surface diffusion was slower than the fluid film diffusion.

GRAPHICAL ABSTRACT

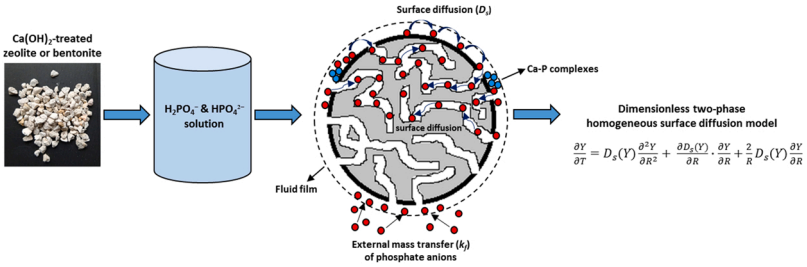

ARTICLE INFO

Keywords:
Phosphate
Bentonite
Zeolite
Surface diffusion
Mass transfer
Modeling

ABSTRACT

Adsorption of phosphate phosphorus (PO_4-P) from wastewater onto eco-friendly geosorbents has gained great attention aiming at recovering an essential nutrient for crop production. Notably, the literature on PO_4-P aqueous-phase adsorption kinetics is limited to the application of either empirical reaction-based models lacking a physical significance or over-simplified diffusion-based models frequently used outside their applicability area. In this study, equilibrium and kinetic experiments are presented under a wide range of phosphate concentrations (50–500 mg P/L) using sustainable and low-cost modified adsorbents. The kinetics of PO_4-P adsorption from aqueous solutions onto $Ca(OH)_2$-treated zeolite (CaT-Z) and bentonite (CaT-B) was analyzed by a dimensionless two-phase homogeneous surface diffusion model (TP-HSDM) assuming constant diffusivity coupled with the double selectivity isotherm equation (DSM). The TP-HSDM fit to the data at four initial P concentrations (50, 100, 200 and 300 mg/L) resulted in an average relative error of 14.6% and 17.4% from the experimental data for CaT-Z and CaT-B, respectively. The average surface diffusion coefficient (D_s) ranged from 2.5×10^{-10} to 8.7×10^{-10} cm^2/s for CaT-Z and from 1.6×10^{-10} to 4.78×10^{-9} cm^2/s for CaT-B. The external mass transfer coefficient (k_f) ranged from 2.72×10^{-4} to 8.38×10^{-4} cm/s for CaT-Z and from 5.63×10^{-4} to 2.24×10^{-3} cm/s for CaT-B. The dimensionless Biot (Bi) number exhibited values in the order of magnitude of 10^5 indicating that the intraparticle diffusion is the controlling mass transfer mechanism for both materials.

* Corresponding author.

https://doi.org/10.1016/j.colsurfa.2022.130805
Received 10 October 2022; Received in revised form 15 December 2022; Accepted 16 December 2022
Available online 21 December 2022

Table 1
Effective diffusion coefficients of phosphate adsorption in batch process estimated by various simplified diffusion models in the literature.

Adsorbent	Contact time, particle size, initial P concentration	Diffusion model	Film mass transfer coefficient (cm/s)	Effective diffusion coefficient (cm^2/s)	Reference
$Ca(OH)_2$ treated zeolite (CaT-Z)	98 d, 0.5–1 mm, 50–500 mg/L	TP-HSDM	$2.72 \times 10^{-4} - 8.38 \times 10^{-4}$	2.5×10^{-10} - 8.7×10^{-10}	This study
$Ca(OH)_2$ treated bentonite (CaT-B)	98 d, 0.5–1 mm, 50–500 mg/L	TP-HSDM	5.63×10^{-4} - 2.24×10^{-3}	1.6×10^{-10} - 4.78×10^{-9}	This study
Microporous drinking water treatment residual (Fe-WTR)	80 d, < 2 mm (9 μm)[a]	Analytical solution	–	4.0×10^{-15}	[26]
Fe-loaded granular activated carbon	7 d, 1.4–2 mm, 4–50 mg/L	Fick's second law	–	8.26×10^{-9}	[28]
Synthetic zeolite (HUD zeolite)	8 h, 0.15–0.30 mm, 50–200 mg/L	Analytical solution	0.90×10^{-3} - 1.86×10^{-3}	1.19×10^{-11} - 9.51×10^{-11}	[15]
Al^{3+} activated synthetic zeolite (Al^{3+}-HUD zeolite)	8 h, 0.15–0.30 mm, 50–200 mg/L	Analytical solution	1.48×10^{-3} - 2.99×10^{-3}	2.08×10^{-11} - 4.66×10^{-10}	[15]
NaCl and $FeCl_3$ treated clinoptilolite	500 min, < 0.2 mm, 10 mg/L	HPDM	–	4.6×10^{-7} (D_p)[b]	[23]
NaCl and $FeCl_3$ treated clinoptilolite	500 min, < 0.2 mm, 10 mg/L	HPFM	–	1.6×10^{-9} (D_f)[b]	[23]
NaCl and $AlCl_3$ treated clinoptilolite	400 min, < 0.2 mm, 10 mg/L	HPDM	–	8.8×10^{-9}	[22]
NaCl and $AlCl_3$ treated clinoptilolite	400 min, < 0.2 mm, 10 mg/L	HFDM	–	4.9×10^{-6}	[22]
$FeCl_3$ and KCl treated clinoptilolite	180 min, < 74 μm, 14 mg PO_4^{3-}/L	HPDM	–	1.1×10^{-9}	[24]
$FeCl_3$ and KCl treated clinoptilolite	180 min, < 74 μm, 14 mg PO_4^{3-}/L	SPM	2.9×10^{-8}	6.8×10^{-10}	[24]
$MnCl_2$ and KCl treated clinoptilolite	180 min, < 74 μm, 14 mg PO_4^{3-}/L	HPDM	–	2.2×10^{-10}	[24]
$MnCl_2$ and KCl treated clinoptilolite	180 min, < 74 μm, 14 mg PO_4^{3-}/L	SPM	7.4×10^{-8}	2.2×10^{-10}	[24]
$AlCl_3$ and KCl treated clinoptilolite	180 min, < 74 μm, 14 mg PO_4^{3-}/L	HPDM	–	1.1×10^{-9}	[24]
$AlCl_3$ and KCl treated clinoptilolite	180 min, < 74 μm, 14 mg PO_4^{3-}/L	SPM	8.3×10^{-7}	5.0×10^{-10}	[24]
NaOH and $LaCl_3$ treated zeolite	6 h, 150–200 mesh, 5 mg/L	Particle diffusion	–	9.5×10^{-10}	[39]
NaOH and $LaCl_3$ treated zeolite	6 h, 150–200 mesh, 5 mg/L	Film diffusion	–	2.09×10^{-6}	[39]
Zeolitic fly ash (KP1)	5 h, powder[c], 10 and 100 mg/L	HPDM	–	7.6×10^{-10} - 1.1×10^{-9}	[25]
Zeolitic fly ash (KP1)	5 h, powder[c], 10 and 100 mg/L	SPM	9.6×10^{-6} - 1.2×10^{-5}	7.2×10^{-10} - 1.7×10^{-9}	[25]
$CaCl_2$ modified zeolitic fly ash (NaP1)	150 min, 29 ± 1 μm[a], 15 mg/L	HPDM	3.6×10^{-5}	2.0×10^{-10}	[40]
$CaCl_2$ modified zeolitic fly ash (NaP1)	150 min, 29 ± 1 μm[a], 15 mg/L	SPM	8.5×10^{-6}	2.1×10^{-10}	[40]
$MgCl_2$ modified zeolitic fly ash (NaP1)	120 min, 29 ± 1 μm[a], 15 mg/L	HPDM	4.8×10^{-5}	2.5×10^{-10}	[40]
$MgCl_2$ modified zeolitic fly ash (NaP1)	120 min, 29 ± 1 μm[a], 15 mg/L	SPM	1.3×10^{-5}	2.6×10^{-10}	[40]
Fly ash	1500 min (25 h), powder[c], 100 mg/L	HPDM	–	$6.7 \times 10^{-12} - 5.0. \times 10^{-11}$	[21]
Fly ash	1500 min (25 h), powder[c], 100 mg/L	SPM	–	7.6×10^{-12} - 6.4×10^{-11}	[21]
Well-ordered modified kaolinite	120 min, < 40 μm, 5 mmo/L (155 mg/L)	Boyd equation	–	7.2×10^{-11}	[41]
Poorly ordered modified kaolinite	120 min, < 40 μm, 5 mmo/L (155 mg/L)	Boyd equation	–	1.0×10^{-11}	[41]
Modified halloysite	120 min, < 40 μm, 5 mmo/L (155 mg/L)	Boyd equation	–	8.5×10^{-11}	[41]
$Al_2(SO_4)_3$ treated activated alumina (continuous adsorption at 25 °C)	4 h, 0.125–0.177 mm, 0.22 and 0.68 mg/L	Boyd equation	–	9.0×10^{-11}	[42]
$Al_2(SO_4)_3$ treated activated alumina (batch adsorption at 5–25 °C)	4 h, 0.125–0.177 mm, 0.30 mg/L	Boyd equation		9.0×10^{-11} - 2.2×10^{-10}	[42]
Acidic soil (pH 5.8)	14 d,< 2 mm, 200 and 400 mg P/kg soil	Fick's first law	–	2.2×10^{-9} - 13.9×10^{-9}	[43]
Molecular diffusion in free liquid solution	–	–	–	8.9×10^{-6}	[26,43]

[a] Most probable (73%) particle diameter in [26] or average equivalent particle diameter (d_{50} value) in [40] based on laser light scattering (laser diffraction method).
[b] The effective diffusion coefficients are denoted either as D_p (particle diffusion) or D_f (film diffusion) and given in m^2/s. Here, the values were converted to cm^2/s.
[c] The particle size range is not reported. However, it must be in powder form according to the parental or modified material used, namely coal fly ash or zeolitic fly ash derived from alkaline hydrothermal treatment with NaOH (NaP1 zeolite) or KOH (KP1 zeolite).

1. Introduction

Numerous studies on phosphate (PO_4^{3-}) adsorption from aqueous solutions have been published the last decade [1,2], motivated by the environmental concerns to control eutrophication and to find secondary phosphorus (P) sources [1]. The concept of circular economy is in line with the recycling of PO_4-P as an essential nutrient for crop production and the characterization of the non-renewable phosphate rocks as a critical material for industries in European Union [3]. There is a great potential of P recovery from point sources of urban and agro-industrial wastewaters (WW) such as municipal WW treatment plants, food processing plants, storage pools of livestock manure or anaerobically digested effluents [4]. The concentrations of dissolved P range from relative (i) low in secondary treated domestic WW (< 10 mg/L), to (ii) moderate in poultry (23–50 mg/L), winery (35–190 mg/L), olive mill (60–110 mg/L) or slaughterhouse (25–200 mg/L) streams, and (iii) high in raw swine effluents (100–900 mg/L) or source-separated urine from no-mix toilets (470–1000 mg/L) [1,5].

Adsorption process exhibits advantages in terms of effectiveness in low P concentrations and operation flexibility regarding the varying P amounts in wastewater effluents [6]. From the agricultural point of view, abundant and soil-friendly, natural minerals, such as bentonite and zeolite, could be used as one-time adsorbents in P-rich effluents and then as nutrient-loaded soil amendments [2]. Certainly, these materials

are able to improve the soil aeration, water holding and cation exchange capacity as well as to reduce nitrogen losses from applied fertilizers [7,8].

The majority of recent adsorption studies with porous materials have employed various chemical reaction- and diffusion-based kinetic models in order to describe the P adsorption rate. The motivation of this modeling is mostly based on the low computational needs and mathematical complexity, and less on the physical meaning or theoretical assumptions of the models [9,10]. The increasing research interest in P adsorption by porous materials has been reflected in recent review articles [1,2,6]. These contain either separate sections for the adsorption kinetics [6], list tables with the best kinetic model to fit the experimental data [2] or just report the best kinetic models employed for various adsorbents [1]. Generally, these reviews overlook the importance of P diffusion modeling and its gap in the literature, although one of them definitely mentions the internal diffusion as one of the five phosphate sorption mechanisms [2]. The aforementioned reviews and numerous other research articles demonstrate that the reaction-based models of pseudo-first order, pseudo-second order and Elovich as well as the intraparticle diffusion model of Weber-Morris were mostly used. Summarizing, in most studies, P adsorption kinetics were best described by the pseudo-second order model [2,6].

Nevertheless, the analysis of batch adsorption kinetics through empirical chemical reaction-based models is heavily criticized for lacking a physical meaning and a theoretical foundation as they do not take into account mass transport processes outside and inside the sorbent particle [10,11]. Additionally, although these models can be successful descriptive tools, they are not predictive under varying experimental conditions [10]. Another remark is that all these empirical kinetic models do not incorporate the equilibrium behavior of the adsorption system, as described by appropriate isotherm equations [12]. The latter is crucial since adsorption equilibrium and estimated isotherm parameters are fundamental preconditions of the applied kinetic models [13].

During the adsorption of a solute compound on a porous material, the following mass transport phenomena and rate controlling steps are sequentially involved [11,14]: (i) diffusion of the adsorbate from the bulk solution to the solid external surface through the liquid film surrounding the adsorbent particle (the process is denoted as external mass transfer or film diffusion, (ii) intraparticle diffusion (or internal mass transfer) including the mass transfer process of pore diffusion (migration of adsorbate within the pore fluid) and surface diffusion (denoted also as solid phase diffusion), and (iii) physical or chemical adsorption at the active surface sites which is not a rate-limiting step as it is a faster process than the film and intraparticle diffusion [11]. The initial transport of the solute compound in the bulk solution is often not rate limiting in small scale and agitated batch systems due to the diminished liquid film around the solid. The pore diffusion mainly occurs in macropores (width $>$ 50 nm) and is dominated by molecular and Knudsen diffusion [9,15]. Thus, pore diffusion is a mass transfer pathway of the adsorbate to approach the internal binding sites of adsorbent particles. On the other hand, surface diffusion is dominant in micropores and describes the hoping of adsorbate ions or molecules from site to site along the surface of pore walls [15–17].

Surface diffusion is still a challenging topic of the adsorption science [11,17]. Its theoretical understanding requires a knowledge of the surface properties, the interactions between the diffusing compounds and surface functional groups, and the interactions among the diffusing compounds [17]. As frequently mentioned in the literature, both diffusional mass transfer mechanisms (pore and surface diffusion) can be combined to an effective (average) intraparticle diffusion coefficient denoted as D_{eff} [15,18]. Therefore, the modeling of external and internal mass transport phenomena during P adsorption in a batch system using porous solids is important in terms of predicting the adsorption rate, simulating operating conditions and designing full-scale processes [19].

As mentioned above, the most common approach to model the intraparticle diffusion of P in batch adsorption experiments has been the application of the Weber-Morris equation, plotting the adsorption capacity (q_t) against the square root of time ($t^{0.5}$). These studies ignore or at least do not present the underlying, restrictive assumptions of the model such as adsorption in an infinite solution volume (constant liquid phase concentration), absence of external mass transfer resistance and a linear adsorption isotherm [20]. In addition, this model does not provide a solid phase diffusion coefficient (cm^2/s) which is the basic parameter of diffusion mass transfer phenomena [9,19]. Other studies have used oversimplified equations of intraparticle diffusion-based models such as the homogeneous particle or film diffusion model (HPDM or HFDM), shell progressive model (SPM) and Boyd equation, to describe the P adsorption kinetics on coal fly ash, zeolitic fly ash and modified natural zeolites [21–25] (Table 1). The effective diffusion coefficient (D_e) of these models was estimated by linear regression analysis based on the coefficient of determination (R^2) (Table 1). Moreover, the majority of these adsorbents was used in a powder form and tested in aqueous phosphate solutions up to few hours (Table 1). The above-mentioned diffusion models have been developed for “bath of infinite volume” (infinite solution volume) where the initial adsorbate concentration in the bulk fluid remains stable during the sorption process [9,19]. To the best of our knowledge, exceptions are earlier studies using Fe-rich drinking water treatment residuals [26] and Al-activated synthetic zeolite [15] (Table 1) which calculated an effective surface diffusion coefficient of P adsorption applying the analytical solution of Fick’s second law proposed by Crank [27]. This solution assumes a “bath of finite (limited) volume” (batch process) where phosphate concentration decreases with time due to adsorption [15,26]. However, the analytical solution of Crank also assumes a linear adsorption isotherm [13] which was not the case of both adsorption studies. Another exception is the recent adsorption study with Fe-loaded granular activated carbon [28] (Table 1). The authors employed a two-site multilayer (equivalent to the BET isotherm) or a monolayer equilibrium model (analogous to the two-site Langmuir isotherm) in combination with the Fick’s second law for spherical particles in order to predict the P internal mass transfer through numerical solution of partial differential equation [28].

Diffusion-based models combining external mass transfer and surface diffusion and including a non-linear isotherm equation have been presented to describe mainly adsorption of heavy metals and food dyes in batch or continuous systems [18,29–31]. However, to our knowledge, there is no published data on the application of similar models to P adsorption from aqueous solutions. Previous works using $Ca(OH)_2$ treated bentonite (CaT-B) and zeolite (CaT-Z) in granular form have revealed an efficient P adsorption from aqueous solutions, synthetic and real wastewater [32–36]. This treatment has been chosen based on the following arguments and findings:(a) $Ca(OH)_2$ is generally cheaper than $MgCl_2$ or $Mg(OH)_2$ [37] which are widely used for the treatment of phosphate adsorbents, (b) Ca- or Mg-based soil amendments are able to improve the stability of soil structure and hinder the dispersion of soil aggregates as a result of increasing Na^+ or K^+ soil salinity [38], and (c) adsorption of P from aqueous solutions on CaT-Z and CaT-B occurred in a wide range of pH values [32,34]. The adsorption mechanisms and presence of P on both adsorbents was confirmed by analytical techniques such as scanning electron microscopy-energy dispersive spectroscopy (SEM-EDS), electron probe microanalysis (EPMA) and infrared attenuated total reflectance (IR-ATR).

In these studies, the P removal from the liquid phase was observed to be a slow process reaching equilibrium after 5–6 days in real wastewater [35] or longer in aqueous solutions [32,34]. Therefore, a longer contact time should be examined to determine the real equilibrium of the adsorption system. The slow adsorption process and the non-equilibrium characteristics after days are indicative of adsorbate diffusion inside the pores of the adsorbing material [2,26]. Besides, the long duration of adsorption process in porous materials may result in a considerable amount of strongly adsorbed and non-extractable phosphate anions [2]. Also, this point has not been deeply studied in the literature.

The objectives of the present work are to determine: (i) the equilibrium time of P adsorption on modified zeolite (CaT-Z) and bentonite (CaT-B) as well as the resulting isotherms, (ii) the effect of the initial P concentration on the external mass transfer and the overall kinetics, and (iii) the dominant rate-controlling mechanism. To this aim, the adsorption kinetics were modelled by applying a dimensionless two-phase homogeneous surface diffusion model (TP-HSDM) assuming a constant surface diffusivity and coupled with a flexible double selectivity isotherm model. The non-dimensional modeling makes easier its numerical solution and general application on other experimental conditions varying the adsorbent dosage, particle size or volumetric flow rate in fixed bed tests [19]. Finally, analyses of SEM-EDS, specific surface area and porosity were conducted to characterize the P-loaded adsorbents.

2. Materials and methods

2.1. Pretreatment of adsorbing materials

The bentonite and zeolite were commercially purchased. The materials were firstly washed with deionized water (DW) to remove impurities and dust. Subsequently, they dried for 24 h in a temperature-controlled chamber at 60 °C and sieved to a particle size of 0.5–1.19 mm. Based on previous works [32,34], the bentonite and zeolite were contacted with 1 and 0.25 mol/L $Ca(OH)_2$, respectively, using a dosage of 50 g per 0.5 L of $Ca(OH)_2$ solution. After 24 h, the adsorbents were separated from the liquid phase, washed with DW to remove excess $Ca(OH)_2$ particles and finally oven-dried at 60 °C. The $Ca(OH)_2$-treated bentonite and zeolite are denoted as CaT-B and CaT-Z, respectively.

2.2. Batch adsorption tests

The adsorption experiments were performed in batch mode by placing 0.5 g CaT-B or CaT-Z and 50 mL phosphate solution (adsorbent dosage = 10 g/L) in a plastic vial (high-density polyethylene) with 100 mL capacity. The vials were sealed and agitated at 200 rpm using a plate shaker, which was placed in a temperature-controlled chamber at 25 ± 0.5 °C. Phosphate stock solutions of 100, 200 and 500 mg P/L were prepared dissolving the appropriate amount of analytical grade KH_2PO_4 in DW. The stock solution of 100 mg P/L was also used to prepare the solution of 50 mg P/L after appropriate dilution whereas that of 500 mg P/L to prepare the solutions of 300 and 400 mg P/L. The initial pH of 200 mL phosphate solutions was adjusted to values of 7.00–7.05 using a few drops of NaOH (0.5–10 M) and/or HCl (0.5–1 M) before adding the adsorbents. All experiments were conducted in triplicate and their average values are reported.

The adsorption kinetic tests were conducted at initial P concentration of 50, 100, 200, 300, 400 and 500 mg/L. In the initial phase of the experiments, supernatant samples of 50 μL were withdrawn in the first 2, 5, 10, 15 and 30 min in order to study the influence of film diffusion (external mass transfer) on phosphate adsorption. In parallel, separate adsorption mixtures were run to collect samples at 1, 2, 3, 4, 8 and 24 h, and subsequently at 2, 3, 4, 5 and 7 days (d). After the first week, samples were withdrawn at time intervals of 7 or 14 d, and up to 91 or 98 d until the residual phosphate concentration remained unchanged.

The total sampling volume did not exceed 3.6% of the initial working volume (50 mL) in the kinetic test with 50 mg P/L, whereas in the tests with 200–500 mg P/L it was ranged from 1.1% to 2.2%. As applied in previous works [32,34], the supernatant samples were not centrifuged since the granular adsorbents remained on the vial bottom during the process and no differences in P concentration have been observed between centrifuged and non-centrifuged samples.

The adsorption capacity (mg P/g) of CaT-Z or CaT-B at time t (q_t) and equilibrium (q_e) was calculated as follows:

$$q_t = (C_0 - C_t) \bullet V/m \quad (1)$$

$$q_e = (C_0 - C_e) \bullet V/m \quad (2)$$

where C_o, C_e and C_t are the initial P concentration, the P concentration at equilibrium and at time t (mg/L), respectively; V is the volume of the solution (L) and m is the adsorbent mass (g). The removal efficiency (R %) of P from the liquid phase was calculated using the following equation:

$$R(\%) = 100 \bullet (C_0 - C_t)/C_0 \quad (3)$$

2.3. Analytical methods

The residual concentration of P in the aqueous solutions was measured with an UV–VIS spectrophotometer (Hach-Lange DR 2800) at wavelength of 880 nm following the ascorbic acid standard method 4500-P E [44]. All chemicals used were of analytical grade. The characterization of the raw and modified adsorbents by the powder X-ray diffraction (XRD) method and the analytical conditions are described earlier [32,34]. The mineralogy of CaT-B and CaT-Z after adsorption at 500 mg P/L was determined using a SIEMENS X-ray diffractometer (D-5000) at the Centre for Research and Technology Hellas (CERTH) in Ptolemais (Greece) in conjunction with the Diffrac.EVA software 4.1. The morphology, microtexture and in-situ elemental composition of CaT-Z and CaT-B surface after adsorption at 200 and 400 mg P/L was investigated using a JEOL JSM IT 500 LV scanning electron microscope (SEM), equipped with back-scattered imaging capability and coupled with an ULTIM Max energy dispersive spectroscopy system (EDS) at the Institute of Geology and Mineral Exploration (HSGME, Athens). Semi-quantitative elemental analyses and elemental mapping were produced using the AZtecLive v. 6.0 software (Oxford Instruments). Operating conditions were as follows: accelerating voltage 20 kV, beam current 1.5 nA and beam diameter 1–2 mm.

Samples of CaT-Z and CaT-B before and after adsorption at 100, 300 and 400 mg P/L were analyzed by N_2 adsorption/desorption isotherms at temperature of 77 K using a porosity and surface area analyzer (TriStar 3000, Micromeritics, USA). This analysis took place at the CERTH of Thessaloniki (Greece). The total pore volume and average pore diameter of the adsorbents were determined by the Barrett-Joyner-Halenda (BJH) calculation method using the N_2 adsorption branch, whereas the specific surface area by the Brunauer-Emmet-Teller (BET) method using values from the linear segment of the N_2 adsorption isotherm [45–47].

2.4. Adsorption kinetics modeling

The theoretical background of the two-phase concentration-dependent homogeneous surface diffusion model (TP-HSDM) and the numerical methods are reported in recent studies and not repeated here [9,11,19,48].

2.4.1. External mass transfer coefficient

The liquid film diffusion (or external mass transfer) plays a rate-determining role only at the beginning of the adsorption process [13]. The following equation assumes that intraparticle diffusion is negligible in the early stage of the process and the adsorbate transport rate is solely determined by film diffusion [49].

$$\frac{\partial \overline{C}_t}{\partial t} = -k_f a_m m(\overline{C}_t - C_s) \quad (4)$$

where $\overline{C_t}$ and C_s (mg/L) are the average adsorbate concentrations in the liquid phase and at the external surface of the particle ($r = r_p$), respectively. The external mass transfer coefficient (k_f) can be estimated by the following integrating equation for initial condition (at $t \rightarrow 0$), $C_t = C_0$ and $C_s = 0$ [13]:

$$\ln\left(\frac{C_t}{C_0}\right) = -k_f a_m \frac{m}{V} t \tag{5}$$

where $a_m = \frac{3}{r_p \rho_p}$ is the total surface area per adsorbent mass (cm^2/g) in a batch reactor assuming spherical and isotropic particles, V (cm^3) is the liquid volume, m (g) is the adsorbent mass in the batch reactor, r_p (cm) is the mean particle radius and ρ_p (g/cm^3) is the adsorbent particle density. In the present work, the average particle radius of both adsorbents was calculated to be 0.04225 cm as an arithmetic mean of the sieve openings used (0.5–1.12 cm). The particle density was assumed to be 2.18 g/cm^3 for zeolite and 2.79 g/cm^3 for bentonite according to earlier studies [50, 51]. The value of the external mass transfer coefficient (cm/s) is calculated by the slope (equal to $-k_f\, a_m\, m/V$) of the initial linear part of the curve of $ln\ (C_t/C_0)$ against time (t) using a linear regression analysis [13].

2.4.2. Two-phase surface diffusion model

The numerical solutions of the diffusion model equations are based on dimensionless variables such as the average dimensionless concentration in the liquid ($\overline{X}$) and solid phase ($\overline{Y}$) at any time (t):

$$\overline{X} = \frac{\overline{C}_t}{\overline{C}_0} \tag{6}$$

$$\overline{Y} = \frac{\overline{q}_t}{\overline{q}_0} \tag{7}$$

where $\overline{C}_0$ is the initial concentration in the liquid phase at t = 0 and $\overline{q}_0$ is the solid phase concentration (adsorption capacity) at equilibrium calculated for $\overline{C}_0$ [13]. The partition (or distribution) ratio (Λ) for batch reactors is expressed as follows [13,52]:

$$\Lambda = \frac{M \bullet \overline{q}_0}{V_L \bullet \overline{C}_0} \tag{8}$$

where M and V_L are the solid (adsorbent) mass and liquid volume, respectively. The dimensionless time (T) is given by the equation:

$$T = \frac{D_{so} \bullet t}{r_p^2} \tag{9}$$

where r_p is the mean particle radius assuming a spherical shape and D_{so} is the constant solid phase diffusion coefficient (cm^2/s). The dimensionless Biot number (Bi), expressing the ratio of internal and external mass transfer, is calculated as follows [13]:

$$Bi = \frac{k_f \bullet r_p \bullet \overline{C}_0}{D_{so} \bullet \rho_p \bullet \overline{q}_0} \tag{10}$$

where k_f is the external mass transfer coefficient (see Eq. 5) and ρ_p (g/cm^3) is the adsorbent particle density. The equation of the material balance containing the partition ratio Λ is:

$$\overline{Y} = \frac{1}{\Lambda} \bullet (1 - \overline{X}) \tag{11}$$

where $\overline{X}$ and $\overline{Y}$ are the average dimensionless concentrations in the liquid and solid phase (Eqs. 6 and 7), respectively. The mass transfer in the liquid phase can be expressed as:

$$\frac{\partial \overline{X}}{\partial T} = 3 \bullet Bi \bullet (\overline{X} - X_{R=1}) \tag{12}$$

where $X_{R=1}$ is the dimensionless liquid phase concentration at the external solid surface (or liquid-solid interface) and $R = r/r_p$ is the dimensionless distance (radial coordinate) from the particle center. Therefore, when $r = r_p$ then R= 1. According to the material balance (Eq. 11), the mass transfer equation in the liquid phase is transformed to:

$$\frac{\partial \overline{X}}{\partial T} = -3 \bullet \Lambda \bullet Bi \bullet (\overline{X} - X_{R=1}) \tag{13}$$

The mass transfer equation in the solid phase is [11]:

$$\frac{\partial Y}{\partial T} = \frac{1}{R^2} \bullet \frac{\partial}{\partial R}\left[R^2 \bullet D_s(Y) \bullet \frac{\partial Y}{\partial R}\right] \tag{14}$$

where $R = r/r_p$ is the dimensionless radius of the adsorbent particle and r is the distance from the particle center, $D_s(Y)=D_s/D_{so}$ and D_s is the concentration dependent solid phase diffusion coefficient.

The Eq. 11 can expand to [11]:

$$\frac{\partial Y}{\partial T} = D_s(Y)\frac{\partial^2 Y}{\partial R^2} + \frac{\partial D_s(Y)}{\partial R} \bullet \frac{\partial Y}{\partial R} + \frac{2}{R} D_s(Y)\frac{\partial Y}{\partial R} \tag{15}$$

In the case of constant surface diffusion coefficient, $D_s(Y)$ is equal to one. The average concentration in the solid phase is:

$$\overline{Y} = 3 \bullet \int_0^1 Y \bullet R^2 dR \tag{16}$$

The initial conditions for dimensionless time $T = 0$ are $\overline{X}_{T=0} = 1$ and $\overline{Y}_{T=0} = 0$ (dimensionless concentrations in the liquid and solid phase, respectively), whereas the boundary condition at the center of the solid ($R = r/r_p = 0$) is:

$$\left(\frac{\partial Y}{\partial R}\right)_{R=0} = 0 \tag{17}$$

A local equilibrium can occur at the solid-liquid interface ($R = r/r_p$ = 1):

$$Y_{R=1} = f(X_{R=1}) \bullet X_{R=1} = f^{-1}(Y_{R=1}) \tag{18}$$

The combination of mass transfer resistance in the liquid and solid phase is expressed as:

$$g(Y_{R=1}) \bullet \left(\frac{\partial Y}{\partial R}\right)_{R=1} = Bi \bullet (\overline{X} - X_{R=1}) \tag{19}$$

The average surface diffusion coefficient can be given by the following equation:

$$D_{s,aver} = \frac{D_{so}}{\theta_\infty} \bullet \int_0^{\theta_\infty} g(\theta) d\theta = \frac{D_{so}}{\overline{Y}_\infty} \bullet \int_0^{\overline{Y}_\infty} g(Y) d(Y) \tag{20}$$

where $\theta_\infty = Y_s \bullet \overline{Y}_\infty$. The infinity subscribe (∞) denotes average concentrations in the bulk phase at infinite time ($t \to \infty$), i.e. at equilibrium [11].

The material balance at equilibrium is getting:

$$\frac{I}{\Lambda} \bullet (1 - \overline{X}_\infty) = \overline{Y}_\infty = f(\overline{X}_\infty) \tag{21}$$

where $f(\overline{X}_\infty)$ is the equilibrium relationship of the dimensionless solid phase concentration as a function of the dimensionless liquid phase concentration.

The fractional attainment of P equilibrium in the solid phase is given by the equation:

$$U(t) = \frac{\overline{q}}{\overline{q}_\infty} = \frac{\overline{Y}}{\overline{Y}_\infty} = \frac{\overline{C}_0 - \overline{C}_T}{\overline{C}_0 - \overline{C}_\infty} = \frac{1 - (\overline{X}/\overline{X}_{T=0})}{1 - (\overline{X}_\infty/\overline{X}_{T=0})} \tag{22}$$

The solution of the TP-HSDM requires the incorporation of an equilibrium isotherm model which takes into account the heterogeneous surface of CaT-Z and CaT-B, and therefore can describe multisite adsorption processes [11]. The simplest form of the so-called double selectivity isotherm model (DSM) assumes a solid phase consisted of two distinct regions of binding sites with no interaction between them [53, 54]:

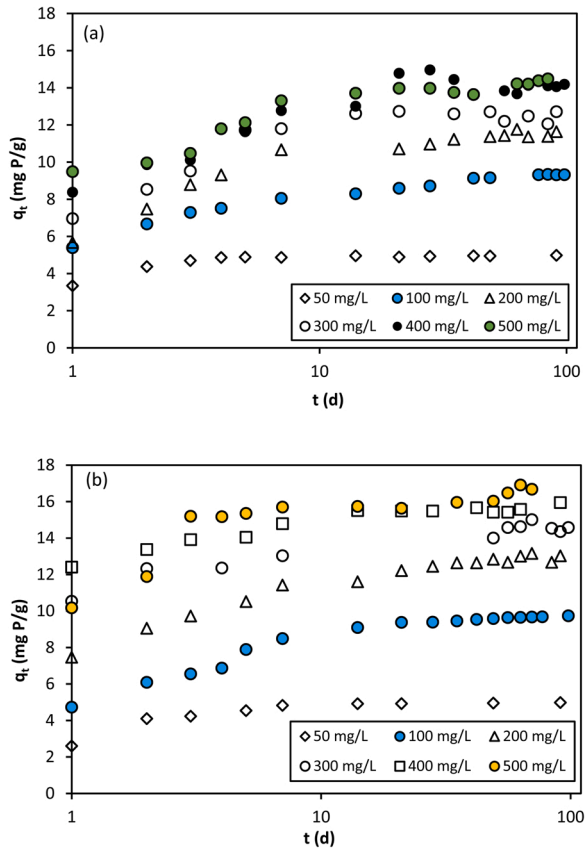

Fig. 1. Variation of P adsorption capacity over time at different initial P concentrations for (a) CaT-Z and (b) CaT-B (adsorbent dosage = 10 g/L, d_p = 0.5–1.19 mm, initial pH = 7.0, T = 25 °C). Logarithmic scale is used for the x-axis to highlight the differences occurred in the first days, whereas cartesian diagrams are presented in Fig. S1a-b.

$$Y = p \bullet \frac{K_1 \bullet X}{1 + (K_1 - 1) \bullet X} + (1 - p) \bullet \frac{K_2 \bullet X}{1 + (K_2 - 1) \bullet X} \quad (23)$$

where K_1 and K_2 are the equilibrium constants and p is the binding sites proportion on the solid surface. This model is highly flexible since it can describe equilibrium data of various shapes including sigmoidal (S-shaped) and Langmurian isotherms [11,19].

The fitting of the DSM isotherm model on the experimental equilibrium values and the calculation of its parameters (all > 0) were performed minimizing the error function of the residual sum of squares (*RSS*):

$$RSS = \sum_{i=1}^{n} (Y_{\exp,i} - Y_{\mathrm{mod},i})^2 \quad (24)$$

where Y_{exp} and Y_{mod} are the experimental and model calculated values of the dimensionless solid phase concentration at equilibrium. The minimization of *RSS* was carried out via the GRG non-linear solving method of the Microsoft Excel Solver tool [11].

The TP-HSDM for constant diffusivity was applied on the experimental data varying the fitting variables D_s and k_f. The average relative error (%) was used to evaluate the model fitting quality between the experimental (U_{exp}) and model (U_{mod}) predicted values of fractional attainment of P equilibrium $U(T)$:

$$ARE = 100 \bullet \frac{ABS[U(T)_{\exp} - U(T)_{\mathrm{mod}}]}{U(T)_{\exp}} \quad (25)$$

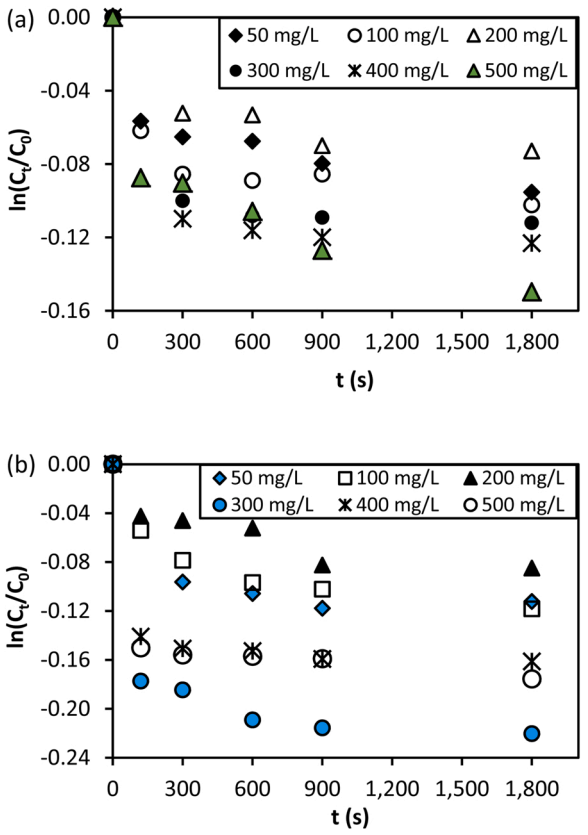

Fig. 2. Logarithmic dimensionless concentration of P during the first 30 min of adsorption on (a) CaT-Z and (b) CaT-B for the determination of the external mass transfer coefficient k_f (adsorbent dosage = 10 g/L, d_p = 0.5–1.19 mm, initial pH = 7.0, T = 25 °C).

Table 2
Liquid and solid phase concentrations of P at equilibrium used for the normalization of the TP-HSDM.

	CaT-Z			CaT-B		
C_0 (mg P/L)	C_e (mg P/L)	q_e (mg P/g)	Equilibrium time (d)	C_e (mg P/L)	q_e (mg P/g)	Equilibrium time (d)
50	0.17	4.98	21–91	0.19	4.98	21–91
100	6.72 ± 0.12	9.33 ± 0.01	77–98	3.39 ± 0.19	9.66 ± 0.02	56–77
200	85.07 ± 1.68	11.49 ± 0.17	49–91	71.71 ± 2.08	12.83 ± 0.21	35–91
300	174.85 ± 2.54	12.51 ± 0.25	14–91	153.87 ± 2.14	14.61 ± 0.21	56–98
400	259.32 ± 2.46	14.07 ± 0.25	35–98	244.41 ± 1.75	15.56 ± 0.17	14–91
500	356.77 ± 1.36	14.32 ± 0.14	63–84	334.79 ± 3.77	16.52 ± 0.38	49–70

3. Results and discussion

3.1. Effect of initial P concentration on equilibrium time

Although the equilibrium was approached slowly after 21–35 d (Fig. 1a-b or Fig. S1a-b), more than 86% of the equilibrium adsorption capacities (q_e) of both materials (Table 2) were attained in the first seven days. For example, this percentage at 400 and 500 mg P/L amounted to 91–93% for CaT-Z and 95% for CaT-B. In all kinetic runs except that at 50 mg P/L, the equilibrium concentrations of P in the liquid (C_e) and solid phase (q_e) (Table 2) were determined as an average of values in the last time intervals, including measurements of at least three weeks

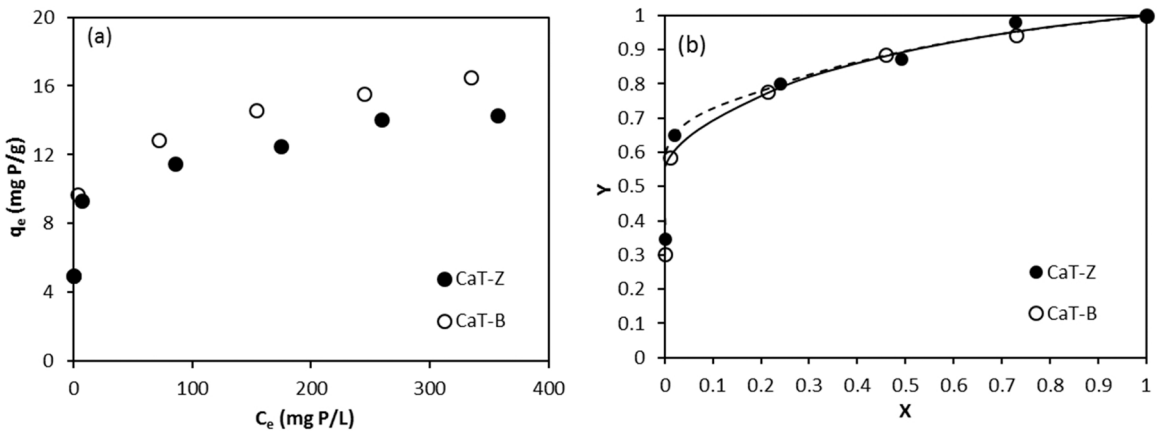

Fig. 3. (a) Experimental equilibrium data of P adsorption on CaT-Z and CaT-B and (b) fitting of the double selectivity isotherm model (solid curves) on the dimensionless P concentrations in the liquid (X) and solid (Y) phase for CaT-Z and CaT-B.

Table 3
Parameters of the double selectivity isotherm model applied on the dimensionless equilibrium data (X, Y) of P adsorption onto CaT-Z and CaT-B.

Adsorbent	*r*	K_1	K_2	*RSS*
CaT-Z	0.649	2370	2.41	0.00130
CaT-B	0.393	2.74	1748	0.00014

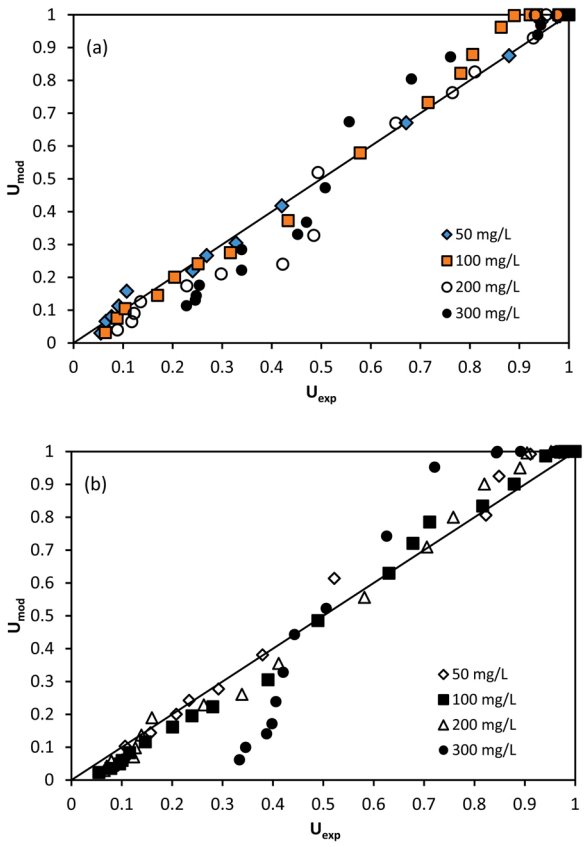

Fig. 4. Fitting quality of the constant diffusivity TP-HSDM for P adsorption on (a) CaT-Z and (b) CaT-B (adsorbent dosage = 10 g/L, initial pH = 7.0, T = 25 °C).

(Table 2). These values were used to normalize the TP-HSDM. The low standard deviation of the C_e values indicates the small differences among the experimental data during the last weeks of the process. To our knowledge, a similar study on long P adsorption kinetics (up to 80 d) was conducted in the work of Makris et al. [26], whereas the experiments of Braun et al. [28] lasted 7 d (Table 1).

Table 4
Mass transfer parameters (k_f, D_s and *Bi*) for P adsorption on CaT-Z and CaT-B at different initial P concentrations (median r_p of both adsorbents = 0.04225 cm).

	CaT-Z			CaT-B		
C_0 (mg P/L)	k_f (cm/s)	D_s (cm^2/s)	*Bi* ($\times 10^5$)	k_f (cm/s)	D_s (cm^2/s)	*Bi* ($\times 10^5$)
50	6.26×10^{-4}	2.50×10^{-10}	2.82	6.93×10^{-4}	1.60×10^{-10}	3.26
100	8.38×10^{-4}	6.30×10^{-10}	2.81	9.91×10^{-4}	3.10×10^{-10}	4.29
200	2.72×10^{-4}	5.60×10^{-10}	1.75	5.63×10^{-4}	6.20×10^{-10}	1.99
300	5.54×10^{-4}	8.70×10^{-10}	2.75	2.24×10^{-3}	4.78×10^{-9}	1.29

Based on the estimated q_e values (Table 2), CaT-B adsorbed more P than CaT-Z at initial concentrations higher than 200 mg/L. The adsorption capacity of CaT-Z seems to approach a plateau at 400 and 500 mg P/L with 14.07 and 14.32 mg P/g, respectively. In contrast, the corresponding q_e values of CaT-B (15.56 and 16.52 mg P/g) differ about 1 mg/g between each other. The observed differences could be associated with the mineral composition of the adsorbents, a scenario that needs further investigation. One of the main mineral phases of bentonite, being a phyllosilicate clay, is montmorillonite which is able to absorb water molecules between its sheets [55]. As a result the layers of montmorillonite can expand, a phenomenon known as swelling [55]. In this case, more phosphate anions could enter the $Ca(OH)_2$ modified interlayer space (internal surface sites) of montmorillonite along with their adsorption on the modified external surface of CaT-B particles [56]. This is possible since the SEM-EDS analysis of CaT-B in a previous work verified a positive correlation of the adsorbed P (quantified as P_2O_5 wt%) with the interlayer calcium ions (as CaO wt%) [32]. Another hypothesis is that the differences in q_e can be due to the treatment of raw bentonite with 1 mol/L $Ca(OH)_2$ instead of 0.25 mol/L $Ca(OH)_2$ for zeolite, although the solubility limit of $Ca(OH)_2$ is about 0.018 M at 23 °C [57].

3.2. Adsorption isotherms and equilibrium modeling

The experimental values of adsorption capacity and residual P concentrations at equilibrium for both adsorbents are illustrated in Fig. 3**a**. The isotherms shape is convex-upward and of Type I indicating a

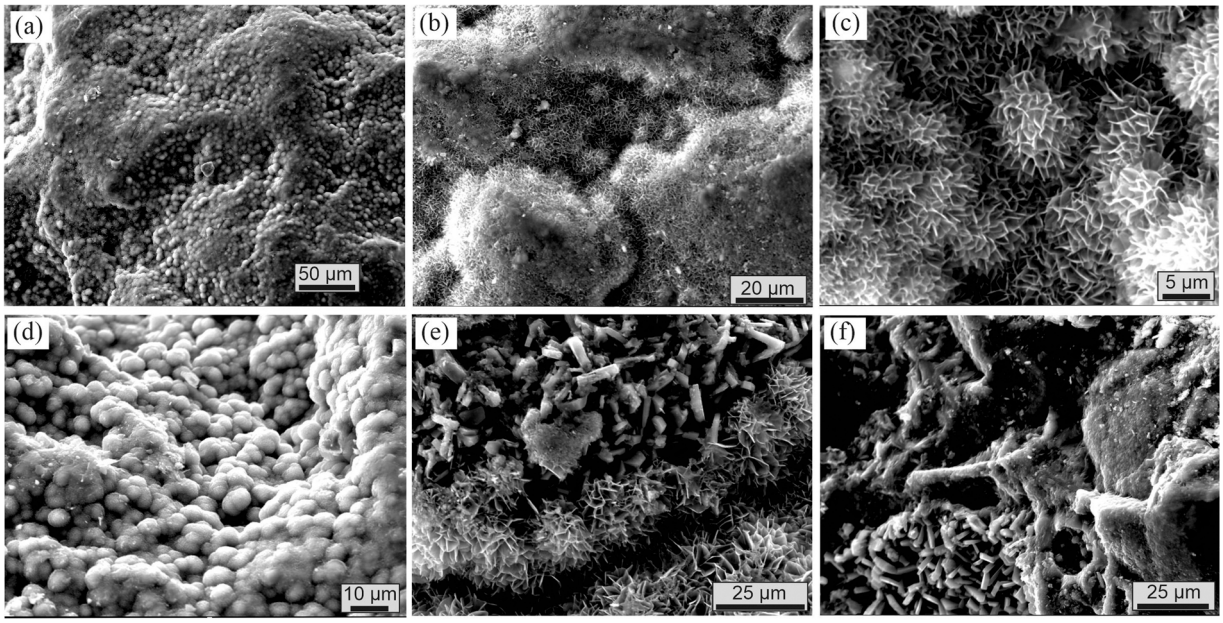

Fig. 5. SEM images of CaT-Z after adsorption at 200 mg P/L (a-d) and 400 mg P/L (e-f). The clinoptilolite occurs as tabular-shaped crystals in (e) and (f).

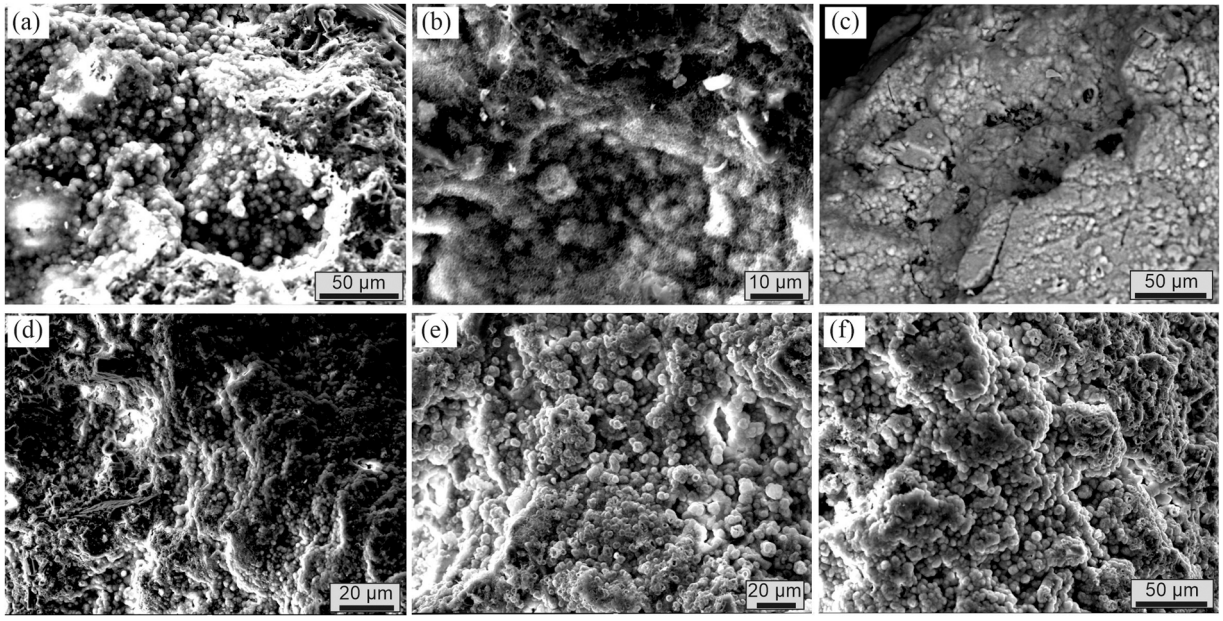

Fig. 6. SEM images of CaT-B after adsorption at 200 mg P/L (a-c) and 400 mg P/L (d-f).

favorable P adsorption on CaT-Z and CaT-B [58]. The parameters of the double selectivity isotherm model (DSM) applied on the dimensionless equilibrium data (Fig. 3**b**) and the *RSS* values used for their estimation are given in Table 3. As shown in Fig. 3**b**, the model fitting describes the experimental data very well for both adsorbents. The non-dimensional DSM has been found to successfully describe convex-upward, linear and sigmoidal adsorption isotherms of heavy metals on zeolite [11,19].

3.3. Results of kinetic modeling and mass transfer parameters

The model fit is shown in Fig. 4a-b. Taking into account the complexity of the TP-HSDM and the quality of similar adsorption models in the literature, the fit is satisfactory for both materials at all P concentrations with overall average relative error of 14.6% for CaT-Z and 17.4% for CaT-B, except that at 300 mg/L for CaT-B ($ARE = 29.6\%$) due to outliers in the fractional attainment region of 0.3–0.4 and 0.7–1 (Fig. 4b). Both average relative errors of the present TP-HSDM application are higher than those (8.56% and 11.2%) derived from the modeling of batch and fixed bed metal adsorption on zeolite [11,19]. A plausible explanation can be the pore blocking by calcium phosphate (Ca-P) phases composing a thin layer on the adsorbents surface or the formation of new pores in this layer. A Ca-P layer has been previously observed in SEM-EDS analyses of loaded CaT-Z (at $C_0 = 100$ mg P/L) [34] and also verified here for both adsorbents (subsection 3.5.2). In an attempt to further investigate the scenario of pore blocking or formation of new pores, the results of specific surface area and porosity analyses are discussed in the subsection 3.5.3. Nevertheless, the TP-HSDM resulted in solid phase diffusion coefficients ranging from 2.5×10^{-10} to 8.7×10^{-10} cm^2/s for CaT-Z and from 1.6×10^{-10} to 4.78×10^{-9} cm^2/s for CaT-B (Table 4), which increased with the increase of

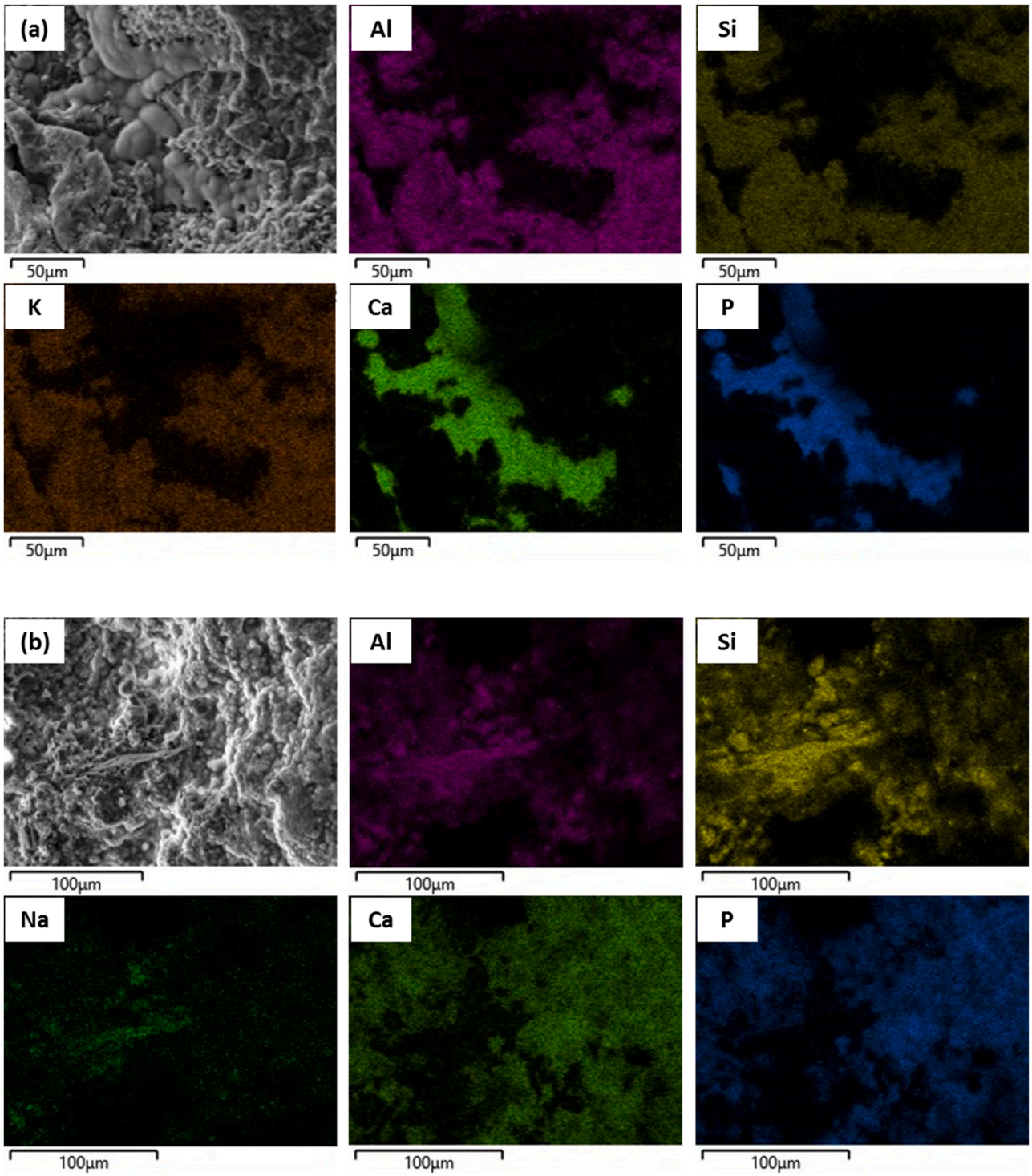

Fig. 7. Qualitative EDS maps of (a) CaT-Z and (b) CaT-B areas after adsorption in 400 mg P/L. Brighter color-scale values indicate higher concentration of the indicated elements.

concentration from 50 to 300 mg P/L (except that at 200 mg/L for CaT-Z). In contrast, for granular activated carbon, Braun et al.[28] estimated by the Fick's second law an effective diffusion coefficient of 8.3×10^{-9} cm^2/s that was independent on P concentration (4–50 mg /L).

In all cases the TP-HSDM showed that Biot number (*Bi*) is higher than 100 to infinite, i.e. the adsorption is controlled by the internal diffusion. To further support this result, the *Bi* number was estimated independently according to Eq. (10). The initial slope of the curve of the logarithmic dimensionless P concentration versus time was estimated using the first three experimental points from time zero to 300 or 600 Section (5-10 min) (Fig. 2). As shown in Table 4, the values of the external mass transfer coefficient (k_f) were found to range from 2.16×10^{-4} to 8.38×10^{-4} cm/s for CaT-Z and from 4.40×10^{-4} to 1.75×10^{-3} cm/s for CaT-B. An earlier study of phosphate adsorption using synthetic zeolite has estimated k_f values in the order of magnitude of 10^{-3} [15]. Values of 10^{-4} to 10^{-3} cm/s are also reported for several adsorption systems in the literature [48]. Based on the resulting surface

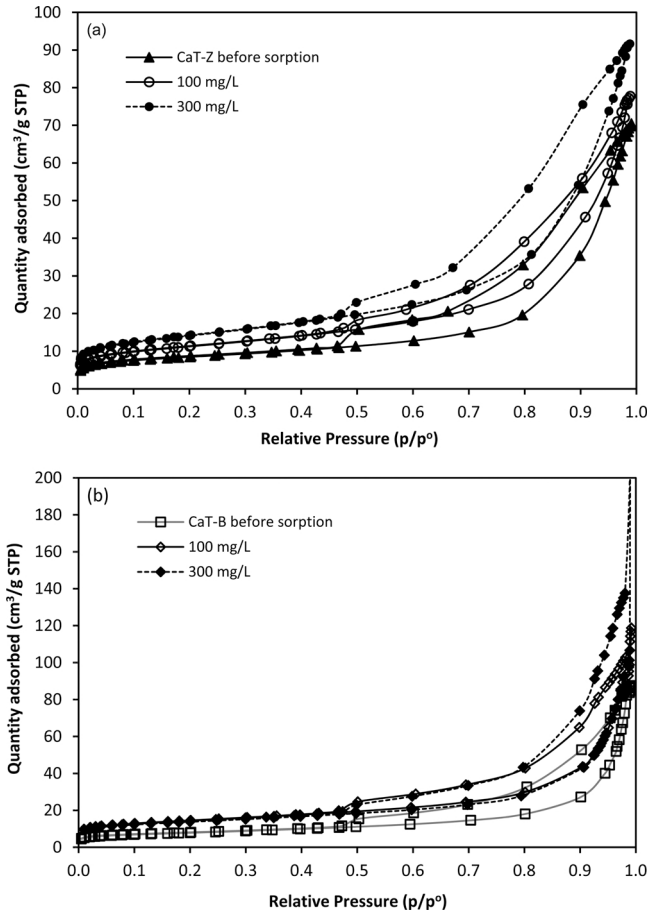

Fig. 8. N_2 adsorption-desorption isotherms of CaT-Z (a) and CaT-B (b) before and after adsorption at 100 and 300 mg P/L. The upper branch of each curve corresponds to the N_2 desorption data.

Table 5
Physical properties of CaT-Z and CaT-B determined by the BET and BJH methods before and after adsorption at 100, 300 and 400 mg P/L.

Adsorbent	mg P/L	N_2 volume adsorbed (cm^3/g STP)*	BET surface area (m^2/g)	Total pore volume (cm^3/g)	Average pore width (nm)
CaT-Z before	–	70.5	31	0.11	9.9
CaT-Z after	100	77.7	40	0.12	8.4
CaT-Z after	300	91.6	50	0.14	8.0
CaT-Z after	400	183.7	36	0.28	29.3
CaT-B before	–	87.6	28	0.13	22.8
CaT-B after	100	118.8	51	0.18	13.1
CaT-B after	300	1102.9	49	0.16	12.5
CaT-B after	400	2264.4	53	0.15	10.3

* At $p/p^o \approx 0.99$.

phase diffusion coefficients, the *Bi* number for all kinetic runs was in the order of magnitude of 10^5 (Table 4). These values are in agreement with the results of the TP-HSDM, i.e. the predominance of the intra-particle surface diffusion as the rate controlling mechanism during P adsorption on both adsorbents.

3.4. Characterization of the adsorbents

3.4.1. XRD characterization

The XRD pattern of CaT-Z after adsorption at 500 mg P/L revealed the phases of clinoptilolite, quartz, sanidine and illite (Fig S2a). The XRD diffractogram of the loaded CaT-B revealed the presence of montmorillonite, anorthite, kaolinite, illite, bytownite (plagioclase) and calcite (Fig S2b). For both adsorbents, the XRD analysis did not reveal any newly formed P-bearing mineral phase (such as Ca-P) suggesting that P adsorption took place either as an amorphous phase or at a modal content below the detection limit of the XRD technique.

3.4.2. SEM-EDS characterization

The SEM-EDS analyses (Table S1) on CaT-Z and CaT-B after adsorption at 200 and 400 mg P/L revealed that large areas of the particles were covered by a thin layer consisted of Ca-P-bearing phases with average CaO and P_2O_5 content of 43.1 and 41.4 wt% on CaT-Z and 44.2 and 38.6 wt% on CaT-B , respectively (Figs. 5 and 6). This layer is an assembly of botryoidal (Fig. 5d for CaT-Z or Fig. 6a, e, f for CaT-B) or concentric clusters composed by μm-sized acicular crystals (Figs. 5b-c, 5e-f). The EDS compositional maps reveal the spatial co-occurrence of Ca and P coupled with the depletion of Si, Al, K (for CaT-Z) and Si, Al, Na (for CaT-B) verifying the neo-formation of the Ca-P-bearing phases (Fig. 7).

3.4.3. Nitrogen adsorption-desorption isotherms

The shape of all N_2 adsorption-desorption isotherms of CaT-Z (Fig. 8a) and CaT-B (Fig. 8b) before and after adsorption were characterized by a hysteresis loop (H3 type) between the adsorption and desorption branches at p/p^o of 0.45–0.99 and a sharp increase in the N_2 adsorbed volume at $p/p^o \approx 0.99$ which indicates the presence of macropores [59]. The isotherms belong to the type IV curve with an almost horizontal part in a wide range of p/p^o suggesting the mesoporous structure (2–50 nm) of both adsorbents [59]. This is confirmed by the values of the average pore diameter (Table 5) derived by the BJH method. As listed in Table 5, CaT-B adsorbed more N_2 volume at $p/p^o \approx 0.99$ than CaT-Z in all cases, suggesting a higher macropore volume for CaT-B and the increasing formation of macropores in both adsorbents when P loading increased. The very high increase in the adsorbed quantity of N_2 to 1102.9 and 2264.4 cm^3/g CaT-B after adsorption at 300 and 400 mg P/L, respectively, indicates that P loading affected the macroporous structure of CaT-B in a different way than that of CaT-Z. However, the N_2 porosimetry as well as the application of BET or BJH methods present restrictions in the presence of micropores regarding the interpretation of isotherm data or the resulting pore size analysis [59]. The pore size distribution of both materials is shown in Fig. S3.

The BET and BJH analyses revealed changes in the specific surface area, the total pore volume and the average pore width (Table 5). After adsorption at 100 and 300 mg P/L, the specific surface area notably increased by 29–61% for CaT-Z and 75–82% for CaT-B, whereas an increase in the total pore volume by 9–27% for CaT-Z and 23–38% for CaT-B was observed. This result must be attributed to the formation of the Ca-P layer on the P-loaded particles (Figs. 5 and 6), providing an additional surface area and pore volume [60]. However, after adsorption at 400 mg P/L, the surface area of CaT-B slightly increased (53 m^2/g), whereas that of CaT-Z notably decreased (36 m^2/g).

On the other hand, the average pore diameter of both adsorbents decreased after adsorption at 100 and 300 mg P/L, and most notably for CaT-B by 42–45% (Table 5) which supports the hypothesis of pore blocking by complexes of Ca-P. This decreasing trend remained only for CaT-B after adsorption at 400 mg P/L, since the average pore width of CaT-Z increased to 29 nm. Clearly, these results are only an indication of the underlying causes of the low quality fit of the model at high concentrations (Fig. 4). Further study is needed to investigate the pore blocking hypothesis by using advanced instrumental analyses such as high-resolution transmission electron microscopy or high-resolution

argon (Ar) sorption porosimetry which can provide structural information about pore shape (geometry), diameter, wall thickness and connectivity [61,62].

4. Conclusions

The batch adsorption kinetics of PO_4-P on modified zeolite and bentonite were successfully described by a non-dimensional two-phase homogeneous surface diffusion model (TP-HSDM) equipped with the double selectivity isotherm model. The model application on the adsorption kinetics at four different initial P concentrations (50, 100, 200 and 300 mg/L) exhibited an average relative error of 14.6% (CaT-Z) and 17.4% (CaT-B) from the experimental data. According to the modeling, the surface phase diffusion coefficient (D_s) increased from 2.5×10^{-10} to 8.70×10^{-10} cm^2/s for CaT-Z and from 1.60×10^{-10} to 4.78×10^{-9} cm^2/s for CaT-B with increasing initial P concentration. For both adsorbents, the *Bi* number values indicated that the internal surface diffusion was slower than the fluid film diffusion, being the controlling mass transfer resistance during P adsorption. The model can contribute to the understanding of the liquid-solid adsorption processes in porous geosorbents avoiding incorrect approaches, uncritically repeated in the literature and based on oversimplified kinetic models. Further investigation is needed to apply a TP-HSDM of variable diffusivity on P adsorption data and to elucidate how the formation of the Ca-P layer on the adsorbents surface affects the porous structure and the mass transfer modeling.

CRediT authorship contribution statement

Dimitris Mitrogiannis: Conceptualization, Methodology, Investigation, Writing – original draft. **Maria Psychoyou:** Validation, Resources. **Ioannis Baziotis:** Validation, Visualization, Data curation, Writing – review & editing. **Constantinos Mavrogonatos:** Resources, Visualization, Data curation, Writing – review & editing. **Nikolaos Koukouzas:** Validation, Resources. **Ioannis Anastopoulos:** Validation, Resources. **Marios Fyrillas:** Software. **Vassilis J. Inglezakis:** Methodology, Software, Validation, Writing – review & editing.

Declaration of Competing Interest

The authors declare that they have no known competing financial interests or personal relationships that could have appeared to influence the work reported in this paper.

Data Availability

No data was used for the research described in the article.

Acknowledgements

This research is dedicated to the memory (R.I.P.) of the co-author Marios M. Fyrillas, Professor of Applied Mathematics and Heat Transfer, who developed the numerical methods and computational solutions of the proposed diffusion model. This research did not receive any specific grant from funding agencies in the public, commercial, or not-for-profit sectors.

Appendix A. Supporting information

Supplementary data associated with this article can be found in the online version at doi:10.1016/j.colsurfa.2022.130805.

References

[1] H. Bacelo, A.M.A. Pintor, S.C.R. Santos, R.A.R. Boaventura, C.M.S. Botelho, Performance and prospects of different adsorbents for phosphorus uptake and recovery from water, Chem. Eng. J. 381 (2020), 122566.
[2] P. Loganathan, S. Vigneswaran, J. Kandasamy, N.S. Bolan, Removal and recovery of phosphate from water using sorption, Crit. Rev. Environ. Sci. Technol. 44 (2014) 847–907.
[3] E.C., European Commission, 20 critical raw materials - major challenge for EU industry, Press Release, Brussels (2014).
[4] F. Battista, N. Frison, D. Bolzonella, Energy and Nutrients' recovery in anaerobic digestion of agricultural biomass: an italian perspective for future applications, Energies 12 (2019) 3287.
[5] V. Carrillo, B. Fuentes, G. Gómez, G. Vidal, Characterization and recovery of phosphorus from wastewater by combined technologies, Rev. Environ. Sci. Biotechnol. 19 (2020).
[6] P.S. Kumar, L. Korving, M.C.M. van Loosdrecht, G.J. Witkamp, Adsorption as a technology to achieve ultra-low concentrations of phosphate: Research gaps and economic analysis, Water Res. X 4 (2019).
[7] O. Latifah, O.H. Ahmed, N.M.A. Majid, Enhancing nitrogen availability from urea using clinoptilolite zeolite, Geoderma 306 (2017) 152–159.
[8] A. Dubey, D.R. Mailapalli, Zeolite coated urea fertilizer using different binders: fabrication, material properties and nitrogen release studies, Environ. Technol. Innov. 16 (2019), 100452.
[9] V.J. Inglezakis, M.M. Fyrillas, J. Park, Variable diffusivity homogeneous surface diffusion model and analysis of merits and fallacies of simplified adsorption kinetics equations, J. Hazard. Mater. 367 (2019) 224–245.
[10] K.L. Tan, B.H. Hameed, Insight into the adsorption kinetics models for the removal of contaminants from aqueous solutions, J. Taiwan Inst. Chem. Eng. 74 (2017) 25–48.
[11] V.J. Inglezakis, M.M. Fyrillas, Experimental study of zeolitic diffusion by use of a concentration-dependent surface diffusion model, Heliyon 5 (2019), e02143.
[12] S. Liu, Cooperative adsorption on solid surfaces, J. Colloid Interface Sci. 450 (2015) 224–238.
[13] E. Worch, Adsorption technology in water treatment: fundamentals, processes, and modeling, Walter de Gruyter2012.
[14] K.K. Choy, D.C. Ko, C.W. Cheung, J.F. Porter, G. McKay, Film and intraparticle mass transfer during the adsorption of metal ions onto bone char, J. Colloid Interface Sci. 271 (2004) 284–295.
[15] M.S. Onyango, D. Kuchar, M. Kubota, H. Matsuda, Adsorptive removal of phosphate ions from aqueous solution using synthetic zeolite, Ind. Eng. Chem. Res. 46 (2007) 894–900.
[16] K. Yang, Y. Sun, Structured parallel diffusion model for intraparticle mass transport of proteins to porous adsorbent, Biochem. Eng. J. 37 (2007) 298–310.
[17] I. Medveď, R. Černý, Surface diffusion in porous media: a critical review, Microporous Mesoporous Mater. 142 (2011) 405–422.
[18] M. Kavand, E. Fakoor, S. Mahzoon, M. Soleimani, An improved film–pore–surface diffusion model in the fixed-bed column adsorption for heavy metal ions: single and multi-component systems, Process Saf. Environ. Prot. 113 (2018) 330–342.
[19] V. Inglezakis, M. Fyrillas, M. Stylianou, Two-phase homogeneous diffusion model for the fixed bed sorption of heavy metals on natural zeolites, Microporous Mesoporous Mater. 266 (2018) 164–176.
[20] M. Schwaab, E. Steffani, E. Barbosa-Coutinho, J.B.S. Júnior, Critical analysis of adsorption/diffusion modelling as a function of time square root, Chem. Eng. Sci. 173 (2017) 179–186.
[21] M. Hermassi, C. Valderrama, N. Moreno, O. Font, X. Querol, N.H. Batis, J. L. Cortina, Fly ash as reactive sorbent for phosphate removal from treated waste water as a potential slow release fertilizer, J. Environ. Chem. Eng. 5 (2017) 160–169.
[22] D. Guaya, C. Valderrama, A. Farran, C. Armijos, J.L. Cortina, Simultaneous phosphate and ammonium removal from aqueous solution by a hydrated aluminum oxide modified natural zeolite, Chem. Eng. J. 271 (2015) 204–213.
[23] D. Guaya, C. Valderrama, A. Farran, J.L. Cortina, Modification of a natural zeolite with Fe(III) for simultaneous phosphate and ammonium removal from aqueous solutions, J. Chem. Technol. Biotechnol. 91 (2016) 1737–1746.
[24] D. Guaya, M. Hermassi, C. Valderrama, A. Farran, J.L. Cortina, Recovery of ammonium and phosphate from treated urban wastewater by using potassium clinoptilolite impregnated hydrated metal oxides as N-P-K fertilizer, J. Environ. Chem. Eng. 4 (2016) 3519–3526.
[25] M. Hermassi, C. Valderrama, O. Font, N. Moreno, X. Querol, N.H. Batis, J. L. Cortina, Phosphate recovery from aqueous solution by K-zeolite synthesized from fly ash for subsequent valorisation as slow release fertilizer, Sci. Total Environ. 731 (2020), 139002.
[26] K.C. Makris, H. El-Shall, W.G. Harris, G.A. O'Connor, T.A. Obreza, Intraparticle phosphorus diffusion in a drinking water treatment residual at room temperature, J. Colloid Interface Sci. 277 (2004) 417–423.
[27] J. Crank, The mathematics of diffusion, Oxford university press1979.
[28] J.C. Braun, C.E. Borba, M. Godinho, D. Perondi, J.M. Schontag, B.M. Wenzel, Phosphorus adsorption in Fe-loaded activated carbon: two-site monolayer equilibrium model and phenomenological kinetic description, Chem. Eng. J. 361 (2019) 751–763.
[29] G.L. Dotto, C. Buriol, L.Ad.A. Pinto, Diffusional mass transfer model for the adsorption of food dyes on chitosan films, Chem. Eng. Res. Des. 92 (2014) 2324–2332.

[30] P. Souza, G. Dotto, N. Salau, Detailed numerical solution of pore volume and surface diffusion model in adsorption systems, Chem. Eng. Res. Des. 122 (2017) 298–307.
[31] V. Russo, R. Tesser, M. Trifuoggi, M. Giugni, M. Di Serio, A dynamic intraparticle model for fluid–solid adsorption kinetics, Comput. Chem. Eng. 74 (2015) 66–74.
[32] G. Markou, V.J. Inglezakis, D. Mitrogiannis, I. Efthimiopoulos, M. Psychoyou, P. Koutsovitis, K. Muylaert, I. Baziotis, Sorption mechanism(s) of orthophosphate onto $Ca(OH)_2$ pretreated bentonite, RSC Adv. 6 (2016) 22295–22305.
[33] G. Markou, D. Mitrogiannis, V. Inglezakis, K. Muylaert, N. Koukouzas, N. Tsoukalas, E. Kamitsos, D. Palles, I. Baziotis, Ca(OH)2 pre-treated bentonite for phosphorus removal and recovery from synthetic and real wastewater, CLEAN Soil, Air Water 46 (2018) 1700378.
[34] D. Mitrogiannis, M. Psychoyou, I. Baziotis, V.J. Inglezakis, N. Koukouzas, N. Tsoukalas, D. Palles, E. Kamitsos, G. Oikonomou, G. Markou, Removal of phosphate from aqueous solutions by adsorption onto $Ca(OH)_2$ treated natural clinoptilolite, Chem. Eng. J. 320 (2017) 510–522.
[35] D. Mitrogiannis, M. Psychoyou, N. Koukouzas, N. Tsoukalas, D. Palles, E. Kamitsos, A. Pantazidis, G. Oikonomou, I. Baziotis, Phosphate recovery from real fresh urine by $Ca(OH)_2$ treated natural zeolite, Chem. Eng. J. 347 (2018) 618–630.
[36] D. Mitrogiannis, M. Psychoyou, M.E. Kornaros, K. Tsigkou, M. Brulé, N. Koukouzas, D. Alexopoulos, D. Palles, E. Kamitsos, G. Oikonomou, A. Papoutsa, S. Xydous, I. Baziotis, Calcium-modified clinoptilolite as a recovery medium of phosphate and potassium from anaerobically digested olive mill wastewater, Environ. Sci. Pollut. Res 27 (2020) 2977–2991.
[37] D.G. Randall, M. Krähenbühl, I. Köpping, T.A. Larsen, K.M. Udert, A novel approach for stabilizing fresh urine by calcium hydroxide addition, Water Res. 95 (2016) 361–369.
[38] X. Liang, P. Rengasamy, R. Smernik, L.M. Mosley, Does the high potassium content in recycled winery wastewater used for irrigation pose risks to soil structural stability? Agric. Water Manag. 243 (2021), 106422.
[39] Y. He, H. Lin, Y. Dong, Q. Liu, L. Wang, Simultaneous removal of ammonium and phosphate by alkaline-activated and lanthanum-impregnated zeolite, Chemosphere 164 (2016) 387–395.
[40] X. You, C. Valderrama, J.L. Cortina, Simultaneous recovery of ammonium and phosphate from simulated treated wastewater effluents by activated calcium and magnesium zeolites, J. Chem. Technol. Biotechnol. 92 (2017) 2400–2409.
[41] J. Matusik, Arsenate, orthophosphate, sulfate, and nitrate sorption equilibria and kinetics for halloysite and kaolinites with an induced positive charge, Chem. Eng. J. 246 (2014) 244–253.
[42] T. Hano, H. Takanashi, M. Hirata, K. Urano, S. Eto, Removal of phosphorus from wastewater by activated alumina adsorbent, Water Sci. Technol. 35 (1997) 39–46.
[43] P. Bhadoria, J. Kaselowsky, N. Claassen, A. Jungk, Soil phosphate diffusion coefficients: their dependence on phosphorus concentration and buffer power, Soil Sci. Soc. Am. J. 55 (1991) 56–60.
[44] APHA, AWWA, WEF, Standard methods for the examination of water and wastewater, 22nd edition, American Public Health Association, American Water Works Association, Water Environment Federation, Washington DC, USA, (2012).
[45] S. Brunauer, P.H. Emmett, E. Teller, Adsorption of gases in multimolecular layers, J. Am. Chem. Soc. 60 (1938) 309–319.
[46] E.P. Barrett, L.G. Joyner, P.P. Halenda, The determination of pore volume and area distributions in porous substances. I. Computations from nitrogen isotherms, J. Am. Chem. Soc. 73 (1951) 373–380.
[47] A.R. Zimmerman, K.W. Goyne, J. Chorover, S. Komarneni, S.L. Brantley, Mineral mesopore effects on nitrogenous organic matter adsorption, Org. Geochem. 35 (2004) 355–375.
[48] V.J. Inglezakis, M. Balsamo, F. Montagnaro, Liquid–solid mass transfer in adsorption systems—an overlooked resistance? Ind. Eng. Chem. Res. 59 (2020) 22007–22016.
[49] T. Furusawa, J. Smith, Fluid-particle and intraparticle mass transport rates in slurries, Ind. Eng. Chem. Fundam. 12 (1973) 197–203.
[50] R. Barrer, R. Papadopoulos, L. Rees, Exchange of sodium in clinoptilolite by organic cations, J. Inorg. Nucl. Chem. 29 (1967) 2047–2063.
[51] H. Komine, Simplified evaluation for swelling characteristics of bentonites, Eng. Geol. 71 (2004) 265–279.
[52] D.M. Ruthven, Principles of Adsorption and Adsorption Processes, John Wiley & Sons, 1984.
[53] F. Pepe, D. Caputo, C. Colella, The double selectivity model for the description of ion-exchange equilibria in zeolites, Ind. Eng. Chem. Res. 42 (2003) 1093–1097.
[54] O. Bricio, J. Coca, H. Sastre, Effect of the heterogeneity of macroporous styrene-DVB resins on ion-exchange equilibria, Solvent Extr. Ion.-. Exch. 15 (1997) 647–664.
[55] S. Malamis, E. Katsou, A review on zinc and nickel adsorption on natural and modified zeolite, bentonite and vermiculite: examination of process parameters, kinetics and isotherms, J. Hazard. Mater. 252–253 (2013) 428–461.
[56] L. Borgnino, C.E. Giacomelli, M.J. Avena, C.P. De, Pauli, Phosphate adsorbed on Fe (III) modified montmorillonite: surface complexation studied by ATR-FTIR spectroscopy, Colloids Surf. A Physicochem. Eng. Asp. 353 (2010) 238–244.
[57] S. Kilic, G. Toprak, E. Ozdemir, Stability of $CaCO_3$ in $Ca(OH)_2$ solution, Int. J. Miner. Process. 147 (2016) 1–9.
[58] S. Brunauer, L.S. Deming, W.E. Deming, E. Teller, On a theory of the van der waals adsorption of gases, J. Am. Chem. Soc. 62 (1940) 1723–1732.
[59] M. Thommes, K. Kaneko, A.V. Neimark, J.P. Olivier, F. Rodriguez-Reinoso, J. Rouquerol, K.S. Sing, Physisorption of gases, with special reference to the evaluation of surface area and pore size distribution (IUPAC Technical Report), Pure Appl. Chem. 87 (2015) 1051–1069.
[60] J. Lin, Z. Zhang, Y. Zhan, Effect of humic acid preloading on phosphate adsorption onto zirconium-modified zeolite, Environ. Sci. Pollut. Res 24 (2017) 12195–12211.
[61] M. Kruk, M. Jaroniec, Y. Sakamoto, O. Terasaki, R. Ryoo, C.H. Ko, Determination of pore size and pore wall structure of MCM-41 by using nitrogen adsorption, transmission electron microscopy, and X-ray diffraction, J. Phys. Chem. B 104 (2000) 292–301.
[62] J. Kenvin, S. Mitchell, M. Sterling, R. Warringham, T.C. Keller, P. Crivelli, J. Jagiello, J. Pérez-Ramírez, Quantifying the complex pore architecture of hierarchical faujasite zeolites and the impact on diffusion, Adv. Funct. Mater. 26 (2016) 5621–5630.